Study and Characterization of LiF Thin Film Combined with a Silicon Detector for Neutron Metrology

H. Brahimi[a,*], A. Keffous[b], N. Haine[c], B. Rahal[a] and Y. Larbah[a]

[a] *Nuclear Research Center of Algiers, 02, Boulevard Frantz Fanon, BP 399, 16038, Algiers, Algeria*
[b] *Research Center in Semiconductors Technology for Energy (CRTSE), 02, Bd. Dr. Frantz Fanon, B.P. 140, 7 Merveilles, 16038, Algiers, Algeria*
[c] *Faculty of Physics, University of Sciences and Technology — Houari Boumedienne (USTHB), BP 32, Bab Ezzouar, 16111, Algiers, Algeria*

Received: 19.01.2023 & Accepted: 16.02.2023

Doi: 10.12693/APhysPolA.143.400 *e-mail: h.brahimi@crna.dz

The last decades have seen a lot of work and development on new methods of neutron detection that would replace ^{3}He gas-based detectors, a device widely used due to its efficiency, which is being phased out due to the scarcity of ^{3}He gas and its high cost. The work showed that a combination of inorganic materials (Si, ^{6}LiF) could represent a viable basis for the development of new generations of thermal neutron detectors. This type of device is based on a silicon detector coupled to ^{6}LiF thin film converters. In this work, a model has been developed based on the fabricated silicon detector with a Schottky surface barrier associated with different thicknesses of ^{6}LiF films. To study its behavior as a function of the different film thicknesses, the model was characterized using a thermal neutron flux from the source (AmBe-OB26). Preliminary results show that it is possible to measure low-energy neutrons with an average detection efficiency of about 1%, a sensibility of 10 ± 0.1 cps on the ^{3}H peak, and insensibility to gamma radiation $< 10^{-6}$, with a thin films size of about 2 μm. In this paper, we will present a state of the art of detector design, an evaluation of its characteristics (efficiency, resolution, dead time, proper motion), and a clarification of the influence of other parameters on the shape of the spectrum, highlighting the possibility of improving its detection efficiency to make it high, with a gamma/neutron rejection capability comparable to the ^{3}He gas detector.

topics: ^{6}LiF, silicon, neutron, detection

1. Introduction

In recent decades, a large worldwide research program has been launched to develop new neutron detection technologies. The objective is to replace ^{3}He gas neutron detectors, widely used due to their sensitivities to radiation other than thermal neutrons, for applications in various stator fields (nuclear research, nuclear safety, nuclear fuel, etc.). These detectors are starting to show some shortcomings, notably the scarcity of ^{3}He gas and its high cost [1]. Research into inorganic silicon (Si) and lithium fluoride (LiF) materials has shown that a judicious combination of these two components could provide a viable basis for the development of new generations of thermal neutron detectors. The operating principle of this structure is based on the use of a LiF film that converts neutrons into charged particles that can be measured by a silicon detector [2].

In this work, a principle study of the structure was carried out and proved its feasibility using a silicon Schottky surface barrier detector fabricated from silicon substrate (Siltronic AG FZ-14 N) of different dimensions (1.44 cm^2, 4 cm^2, and 0.7 cm for diameter), to which we combined a LiF thin film of different thicknesses (0.5, 1, 2, 3, 4, and 5 μm) by thermal evaporation technique. The fabricated structure was characterized spectrometrically after irradiations with an AmBe neutron source (OB26/SSDL-CRNA) [3] in order to evaluate its detection efficiency and energy resolution as a function of different LiF film thicknesses. A first analysis of the neutron energy spectra as a function of ^{6}LiF film thickness shows a typical spectrum shape, which allows us to easily distinguish the neutron capture reaction products in lithium-6 (^{6}Li) from the gamma background. This first result is very significant and satisfactory and has shown a relationship between the detection efficiency and the thickness of the film.

Herein, we present the state of the art of a promising and inexpensive method for the fabrication of a thermal neutron detector structure based on a silicon Schottky surface barrier detector associated with a ^{6}LiF film, followed by a discussion of the performance of the structure (detection efficiency, energy resolution, and background noise) as a function of the ^{6}LiF film thickness.

2. The experimental process

The experimental thermal neutron device consists of a silicon detector with a Schottky surface barrier, to which ^{6}LiF conversion thin films of different thicknesses have been added. The detection principle is based on two steps: the first occurs in the conversion film, where the neutron produces high-energy particles ($\alpha, {}^3$H) through exothermic or endothermic inelastic scattering reactions, and the second step takes place in the silicon detector, where the emitted particles deposit their energies in the active volume, leading to the creation of pairs (e^-, e^+) generating an electrical signal proportional to the deposited charge [4].

2.1. Silicon detector

In this work, a model of a Schottky surface barrier detector in silicon was designed according to the principle of charge collection of pairs (electron–hole) generated by the interaction of charged particles (ionization) in silicon and/or under the effect of an electric field, in which the electrons (e^-) are attracted by the anode and the ions (e^+) are collected by the cathode, or an electric current of low intensity is created in the circuit connecting the two electrodes. The detector used must respect the model of Schottky and Mott, who established a relation between the energy difference of the band gap with the Fermi level in the metal ($e\varnothing_{\rm M}$) and the electron affinity ($e\chi_{\rm SC}$) representing the energy difference between the band gap and the conduction band (CB) [5]. The Schottky and Mott model is summarized in the equations below

$$e\varnothing_{\rm M} > e\varnothing_{\rm SC}, \tag{1}$$

$$eV_{\rm bi} = eV_{\rm M} - e\chi_{\rm SC}, \tag{2}$$

$$eV_{\rm bi} = eV_d = e\varnothing_{\rm M} - e\varnothing_{\rm SC} = e\varnothing_{\rm MS}. \tag{3}$$

In Table I, we have given the work output values ($\varnothing_{\rm M}$) for different metal elements with the electron affinity ($\chi_{\rm SC}$) for semiconductor elements.

We have developed our diodes from metals Al and Au with $\varnothing_{\rm M}$ values of 4.28 V and 5.1 V, respectively, and with silicon semiconductor of electronic affinity $\chi_{\rm SC}$ = 4.01 V (see Table I), forming a Schottky contact according to (1).

The fabrication of the Schottky surface barrier detectors of various shapes and sizes has been widely described in many works [6]. The detector used for this work is a prototype of different dimensions, fabricated from a silicon substrate (Siltronic AG FZ-14 N, type N, resistivity 0.7–1.300 kΩ cm, thickness 300 μm). The substrates were previously cleaned with RCA chemical treatment methods and then re-oxidized in an HF (hydrofluoric acid) bath for 5 s [7].

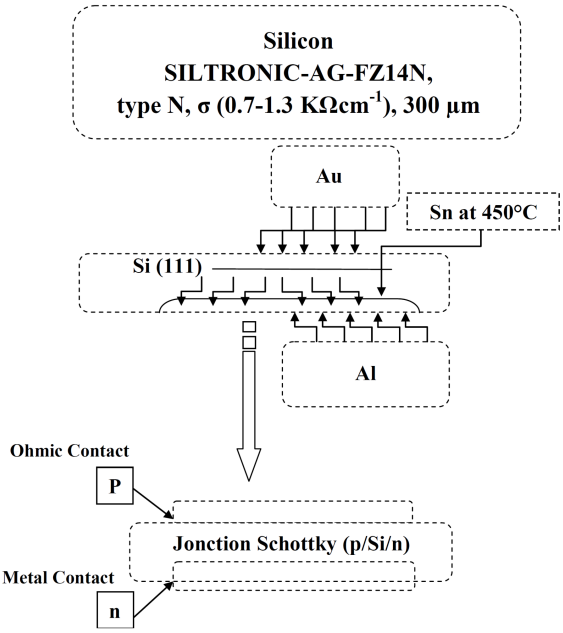

Fig. 1. Manufacturing method of silicon junction detector (n = [p-Si]).

TABLE I

Work functions of some metal/ elements affinity of some semiconductor.

Metals	
Element	Work function $\Phi_{\rm M}$ [V]
Al	4.28
Au	5.1
Semiconductors	
Element	Electron affinity $\chi_{\rm SC}$ [V]
Si	4.01

The Schottky barrier was formed by depositing SnO_2 thin film on a silicon substrate and then diffused by annealing in situ at 450°C. The depth of the zone is measured to be about $\sim$ 10 μm, which is perfect for depletion zone formation, and at this time the structure is of the (n=[p-Si]) type. The ohmic and metallic contacts were formed by Au and Al films. The detectors are made of fully depleted silicon at 80 V and are therefore suitable for use with neutron converters. Figure 1 describes the fabrication procedure of a silicon Schottky surface barrier detector.

2.2. Electrical test

The [p-Si] diodes of the previously developed models:

- diode M1A: [Si-SBD$_{2\ \rm cm\times 2\ cm\times 300\ \mu m}$],
- diode M1B: [Si-SBD$_{1\ \rm cm\times 1\ cm\times 300\ \mu m}$],
- diode M2: [Si-SBD$_{0.7 \rm of \varnothing \times 300\ \mu m}$],

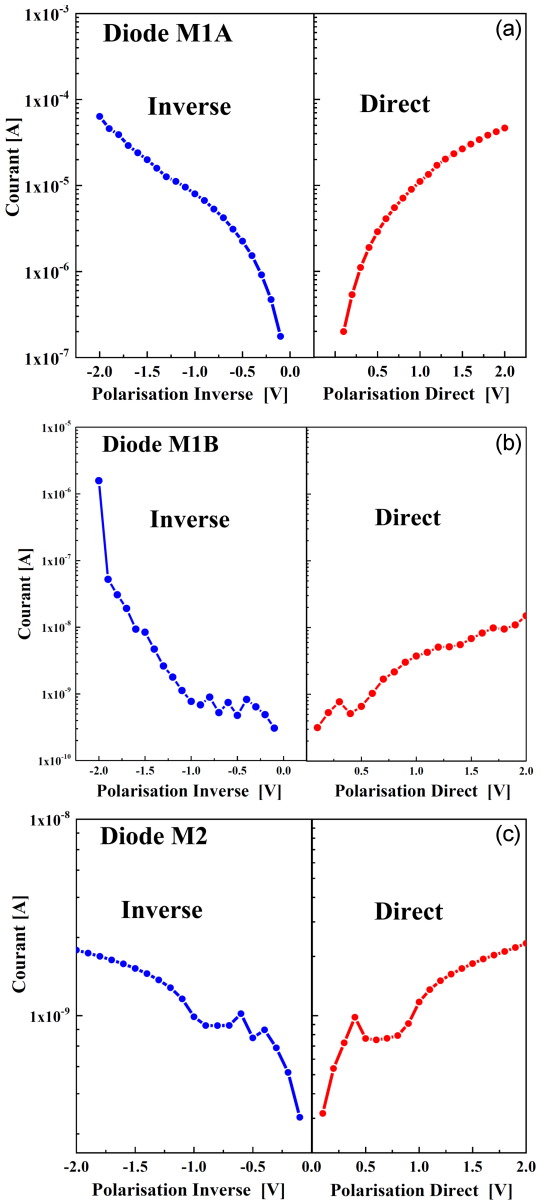

Fig. 2. I–V graph of different diode models: diode M1A, diode M1B, and diode M2.

will be characterized by electrical tests for the measurement of reverse current and output capacitance as a function of bias voltage, $(I\,\mathrm{d}V/C\,\mathrm{d}V)$, at an ambient temperature, using a Keithley 648 instrument. Figure 2 shows the I–V characteristics of the different diode models (Diodes M1A, M1B, and M2) at the reverse and forward bias voltage.

By applying a negative voltage V on the p-side, a leakage current occurs around the p-type region, and a voltage gradient is established in this region, forming a low potential barrier near the high field region of the junction. Electrons are thus injected into the semiconductor volume, forming a leakage current whose value cannot exceed the currents due to thermal generation and diffusion in the junction [8, 9].

The voltage V and potential field ϵ are derived from the relation

$$\frac{\mathrm{d}^2V(x)}{\mathrm{d}x^2} = -\frac{\epsilon(x)}{\epsilon_{\mathrm{SC}}}. \tag{4}$$

The capacity is expressed with relation

$$C = A\left|\frac{\mathrm{d}Q}{\mathrm{d}V}\right| = \frac{e\,\epsilon_{\mathrm{SC}}\,N_d}{2(V_{\mathrm{bi}}-V)} = \frac{\epsilon_{\mathrm{SC}}A}{W}, \tag{5}$$

where N_d coresponds to the density of majority charges, by analogy with p and n type semiconductors. The number of electrons which manage to cross the barrier $e(V_{\mathrm{bi}}-V)$ is given by the relation

$$n_{\mathrm{b}} = N_c \exp\left[\frac{E_c - E_{\mathrm{F}}}{k_{\mathrm{B}}T}\right] \exp\left[-\frac{e(V_{\mathrm{bi}}-V)}{k_{\mathrm{B}}T}\right]. \tag{6}$$

The flow of electrons across the potential barrier is

$$\tfrac{1}{4}\, n_{\mathrm{b}}\langle v\rangle, \tag{7}$$

where $\langle v\rangle$ is the average electron velocity, so the electron current from the semiconductors (SC/M) to the metals is given by

$$I_{\mathrm{SC/M}}\,(V) = \frac{e\,\langle v\rangle A\,N_c}{4} \exp\left[-\frac{e(\varnothing_{\mathrm{b}}-V)}{k_{\mathrm{B}}T}\right]. \tag{8}$$

If the bias voltage is zero, there is a balance between the current M $\rightarrow$ SC and the current SC $\rightarrow$ M, and the current is

$$I_{\mathrm{M/SC}} = -I_{\mathrm{SM}} = -\frac{e\,\langle v\rangle A\,N_c}{4} \exp\left[-\frac{e\varnothing_{\mathrm{b}}}{k_{\mathrm{B}}T}\right]. \tag{9}$$

The analysis of the electrical curves (Fig. 2) highlighted that a number of diodes presents good electrical characteristics, such as a low reverse current (lower than 5 pA), a resistance of about 1.3 kΩ, and a capacitance of about 40 nF for bias voltages from 40 to 80 eV. This can be explained in part by the careful use of the cleaning procedures (RCA) described in the literature. Indeed, F.S. Goulding and W.L. Hansen [10] have established after numerous experiments that these chemical cleaning methods, if correctly applied, eliminate all traces of impurities responsible for the increase in reverse currents. A temperature rise effect on the diode resistance has been observed, making the measurements dependent on the duration of the experiment. To remedy this, it is recommended to install a heat dissipation mechanism in the silicon. We continue this work of characterization of the diodes by tests of detection of alpha particles in order to evaluate their efficiencies of detection and to deduce their energy resolutions.

2.3. Spectrometry test

To make the necessary alpha spectrometry tests, an experimental test bed was used (Fig. 3), consisting of a preamplifier (ORTEC 142B), to which the output of the diode was sent, connected to an amplifier (ORTEC 572) for signal shaping, an ADC (ORTEC 1420) and an MCA interface card, associated with the software (EMCAPLUS, InterWinner Alpha), for data acquisition, reverse biased an 80 V with a time of 1.0 μs for signal shaping.

Fig. 3. Alpha spectrometry with ^{239}Pu standard source, bench test.

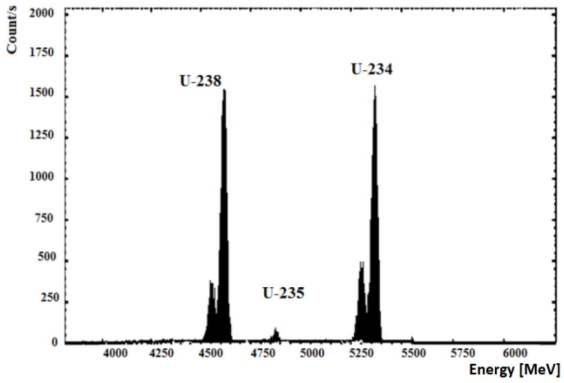

Fig. 4. Alpha spectrum of (^{238}U, ^{235}U, ^{234}U; CEA/LMRI) source, using Si-implanted detector.

Before performing the necessary tests, the electronic modules of the spectrometry chain (amplifier, HV, PZ, preamplifier) described above were first adjusted with the help of an oscilloscope (Philips) and using a manufactured silicon detector model Si-implanted from Eurisys Mesures and using a standard multi-alpha source (^{238}U, ^{234}U, ^{235}U, CEA/LMRI).

Figure 4 represents the alpha spectrum of the multi-alpha source, measured during 600 s. The analysis of the spectrum (Fig. 4) will allow us to fix the parameters of the electronic modules of the chain for the whole duration of the diode spectrometry tests. After having fixed the parameters of the electronic modules of the chain, the diode models (M1A, M1B, and M2) were calibrated using a standard alpha source of uranium (^{238}U, ^{234}U, ^{235}U, CEA/LMRI). Figure 5 shows the alpha spectra of the uranium source, measured for 7200 s.

Figure 6 shows a linear calibration curve of the energy of an alpha particle from the standard ^{239}Pu source as a function of the channel number in the multichannel analyzer. We have established a linear relationship between the channel number read from the spectrum and the energy (E) deposited in the detector.

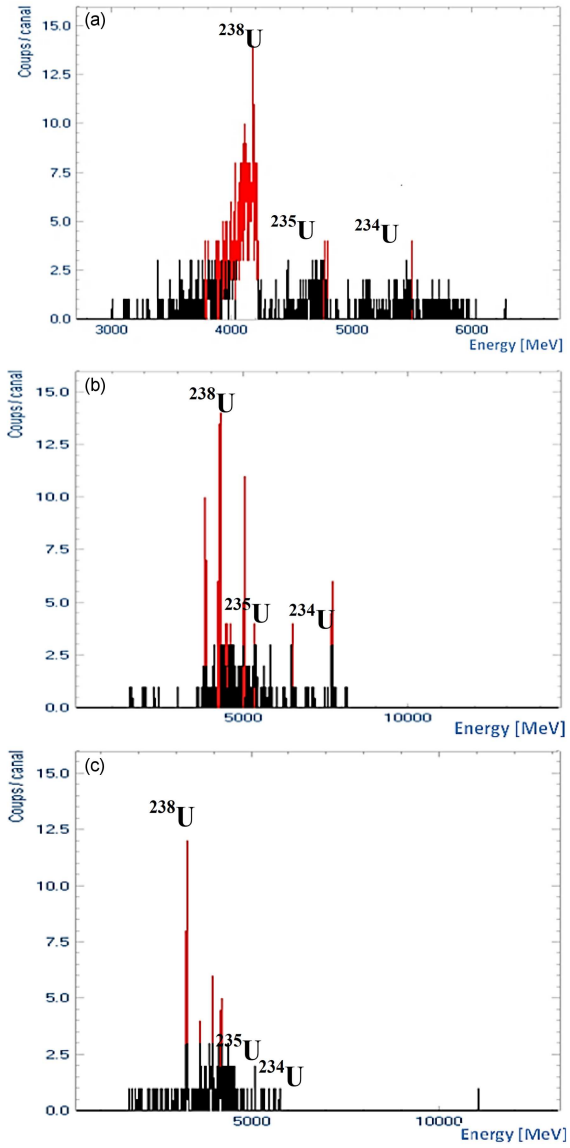

Fig. 5. Alpha spectrum of a multi-alpha source (^{238}U, ^{235}U,^{234}U; CEA/LMRI), measured during 7200s, with detectors diodes: (a) M1A, (b) M1B, and (c) M2.

We will deduce the energies of characteristic alpha spectra of another alpha-emitting radioelement with the following equation

$$E \ \ [\text{MeV}] = 7.3411 \times 10^{-4} N_{\text{canal}} + 9.11 \times 10^{-3}. \tag{10}$$

From the measured alpha spectrum in Fig. 5, we deduced the energy resolution (R [%] = $\frac{\Delta E}{E}$) according to the spectral method.

For each detector model, the energy resolution of the detector is defined by FWHM (full width at half maximum) and expressed in energy units (keV). It is also defined by the ratio of FWHM to the peak center pulse H_0, i.e.,

$$R\ [\%] = \frac{\text{FWHM}}{H_0} = \frac{\Delta E}{E}. \tag{11}$$

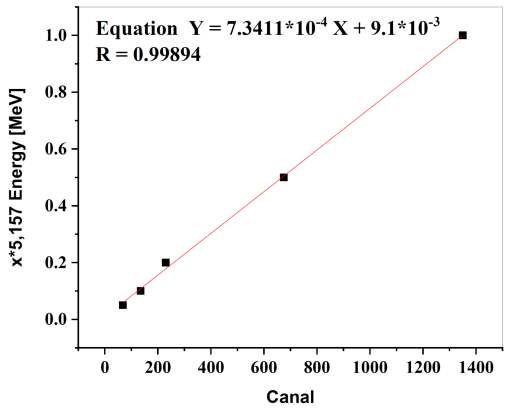

Fig. 6. Calibration line $E = f(c)$ with ^{239}Pu source of detector.

TABLE II

Alpha spectrometry of calibration data test.

Characteristics	Detectors			
	Si-implanted	[Si-SBD$_{2cm\times2cm\times300\mu m}$]	[Si-SBD$_{1cm\times1cm\times300\mu m}$]	[Si-SBD$_{d=0.7\varnothing\times300\mu m}$]
Background	1	50	125	150
Measurement time [s]	7200	7200	7200	7200
Number of counts	1322	953	473	389
Resolution, R [keV]	12	30	80	150
Efficiency (E [%]) Position 1 [cm]	33	25	10	2
n	0.99	0.90	0.75	0.68

In order to access the number of particles emitted by the source, it is necessary to know the detection efficiency (ε), defined by the ratio between the number of events recorded and the number of particles emitted by the source, with the following relation

$$\varepsilon = \frac{\text{number of recorded events}}{\text{number of particles emitted by the source}}, \tag{12}$$

also given as a function of the solid angle according to the relation

$$\varepsilon = \frac{4\pi N}{S\,\Omega}, \tag{13}$$

where S is the number of particles emitted by the source, N is the number of events below the total absorption peak, and Ω is the solid angle [11–13].

The results of the spectrometry tests are summarized in Table II. It is indicated clearly that the [Si-SBD$_{2cm\times2cm\times300\mu m}$] detector has the best characteristics for the detection of alpha particles. By making some modifications to this detector, such as a good cleaning of the silicon surface, we can improve its detection efficiency to reach a maximum of 25% and an energy resolution of at least 30 keV.

2.4. Lithium fluoride (LiF) converters

The second important component of the neutron detector is the neutron conversion film associated with the silicon detector. In this work, the material used to form the conversion film is lithium fluoride, (^{7}LiF; ^{7}Li of 95% and ^{6}Li of 5%) and (^{6}LiF: Mg, P; ^{6}Li of 95% and ^{7}Li of 3%), supplied in powder or crystal form, respectively, by Fluka and Thermo Fisher Scientific. The neutron conversion mechanism in the LiF film exploits the following nuclear reaction (see also Fig. 7) [14] ^{6}Li (n, ^{3}H)^{4}He; ^{3}H (2.73 MeV) +^{4}He (2.05 MeV). Being the only possible decay pathway devoid of the gamma component, the energy spectrum measured by the silicon detector under these conditions will have a typical shape that will discriminate the background component of the products (α and ^{3}H) of the neutron reaction with the ^{6}Li atom.

The kinetic energy (E_α and E_{3H}) of the products of the ^{6}Li reaction were determined computationally using a laboratory reference frame where the direction of the incident neutron is normal to the axis, using the principle of conservation of energy by the relation

$$E_n + Q = E_\alpha + E_{3H}; \quad Q = 4.78 \text{ MeV}. \tag{14}$$

The kinetic energies (E_α) and (E_{3H}) are given by the relations

$$\sqrt{2mE_n} = \sqrt{2m_\alpha E_\alpha}\cos(\delta) + \sqrt{2m_{3H}E_{3H}}\cos(\delta), \tag{15}$$

$$0 = \sqrt{2m_\alpha E_\alpha}\sin(\delta) + \sqrt{2m_{3H}E_{3H}}\sin(\delta), \tag{16}$$

$$E_\alpha = \frac{3}{7}Q + C_1\cos(\theta), \tag{17}$$

$$E_{3H} = \frac{4}{7}Q + C_2\cos(\delta), \tag{18}$$

where E_n is the kinetic energy of the incident neutron, E_α is the kinetic energy of the particle, E_{3H} is the kinetic energy of the triton, C_1 and C_2 are constant, and Q is the nuclear decay energy.

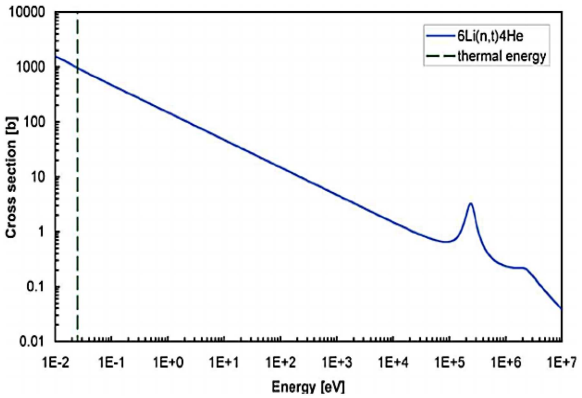

Fig. 7. Cross section of the reaction of ^{6}Li.

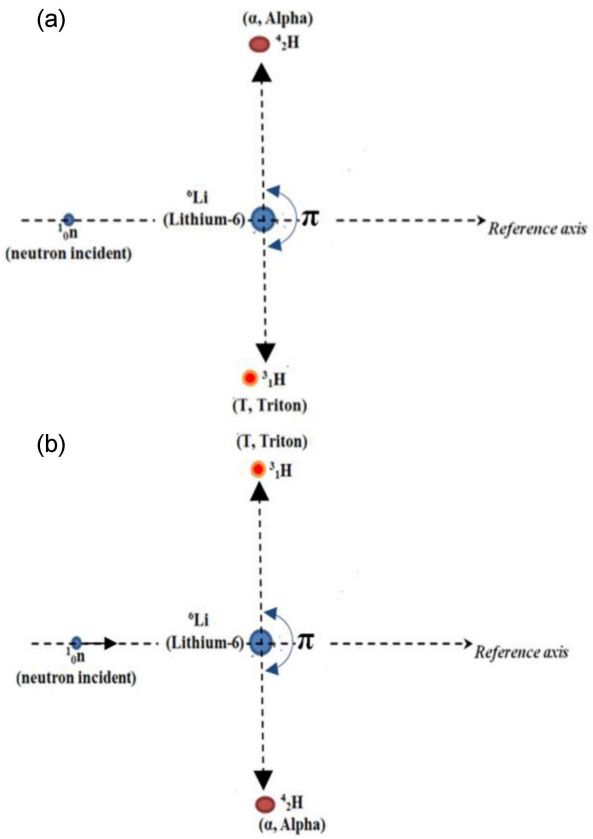

Fig. 8. The kinetics of the nuclear reaction ^{6}Li (n, ^{4}He)^{3}H along a reference axis, emitted in opposite directions at an angle $\theta = \delta + \pi$.

According to (17) and (18), for a thermal neutron of energy (E_n) of 0.025 eV, the kinetics energies of the particles produced from the ^{6}Li reaction are $E_\alpha = 2.052$ MeV and $E_{3\mathrm{H}} = 2.735$ MeV.

In reality, these values of kinetic energies (E_α and $E_{3\mathrm{H}}$) do not correspond to the values of the minimal energies that can reach the alpha and ^{3}H particles during the reaction. The values of the minimum energies, $E_{\alpha\,\mathrm{min}}$ and $E_{3\mathrm{H\,min}}$, can be deduced from the derivatives of the energy functions (E_α, $E_{3\mathrm{H}}$) with respect to the energy of the incident neutron (E_n).

The method of calculating $E_{\alpha\,min}$ and $E_{3\mathrm{H\,min}}$ consists of:

- $\cos(\delta) = -1$, for $\delta = \pi$;
- replacing δ in E_T to calculate E_n for $\mathrm{d}E_T/\mathrm{d}E_\mathrm{n} = 0$.

We found that $E_{3\mathrm{H\,min}} = 2.393$ MeV and $E_{\alpha\,\mathrm{min}} = 1.597$ MeV. This result is very important for the rest of the neutron spectrometry work — it will allow us to discriminate the amplitudes of the neutron measurement spectrum. It tells us how to fix the value of the electronic threshold, which will be very close to and slightly lower than the minimum energy (E_min), taking into account the selectivity of the electronic circuits providing the "threshold" function.

From the energy conservation equation (14) projected on a laboratory reference frame, we obtain equations (16) and (17), and neglecting the component $E_\mathrm{n} = 0.025$ eV for neutrons thermal, the ratio of the two equations makes it possible to write

$$\tan(\theta) = \tan(\delta) \Rightarrow \theta = \delta + k\pi. \tag{19}$$

This implies that the charged particles cannot be emitted in the same direction. Thus, for the reaction ^{6}Li(n, α)^{3}H, the particles (α, ^{3}H) are emitted in opposite directions at an angle of 180°, as shown in Fig. 8.

This result of the study of the emission angle of the charged particles of the ^{6}Li reaction is very important for the calculation of the detection efficiency as a function of the energy of the incident neutrons and of the position of the Si detector for the measurement of (α, ^{3}H) particles [15, 16].

2.5. Development and characterization of LiF films

LiF samples at different thicknesses from 0.5 to 5 μm were prepared by the thermal evaporation method using the evaporator (UNIVEX 300, Leybold Heraeus). The masses of ^{7}LiF (Fluka) and ^{6}LiF:Mg, Cu, P (Thermo Fischer) were deposited on a silicon substrate (Si (111) 4 cm^2 × 300 μm), then subjected to a heat treatment in a temperature range of 300–400°C in order to obtain nanostructured polycrystalline thin films. The thicknesses of the films are controlled by means of the oscillator (quartz) as the evaporation progresses. The LiF films were exhibited to irradiation with a gamma dose of 150 kGy and a neutron fluency of 1.4 × 10^{14} n s cm^2. The samples were characterized by scanning electron microscopy (SEM), energy-dispersive X-ray analysis (EDX), and X-ray diffraction (XRD) for the study of their structural and morphological properties.

The images of LiF thin films deposited by the thermal evaporation method on a silicon substrate at thicknesses up to about 1 μm are shown in Fig. 9a. The images revealed a homogeneous morphological structure and the chemical composition of particles LiF (see Fig. 9b). The chemical composition of the studied thin films was obtained through energy-dispersive X-ray analysis (EDX). Table III shows the EDX analysis values of the concentrations of the main elements that make up these thin films. Particle analysis indicates that they are based on F and other impurities, i.e., O, Al, Cu, and P. It was found that the content of P is the highest, considered the second most important component together with Mg in the material, which can form various lithium phosphates. On the other hand, impurities were found with lower concentrations of Si, Al, and K.

X-ray diffraction (XRD) is a non-destructive analysis that provides detailed information on the chemical composition, crystallographic structure, and microstructure of the material.

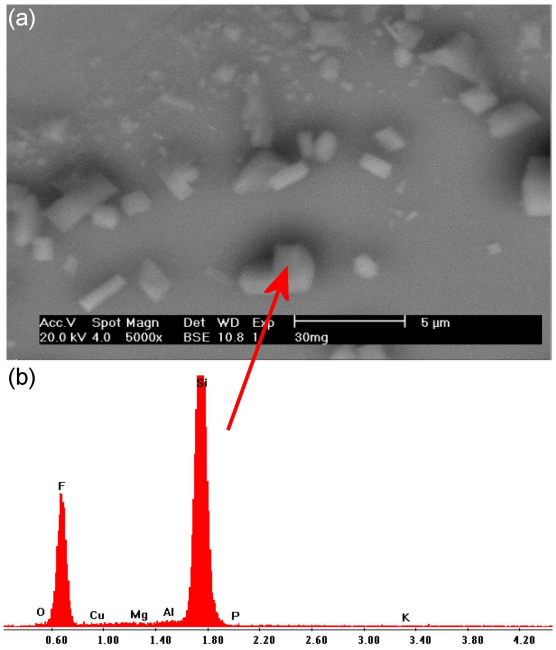

Fig. 9. (a) ESEM image and (b) EDX analysis of LiF thin film irradiated gamma dose 150 kGy.

TABLE III

EDX analysis values of the concentrations of the main elements in the LiF film.

Element	Wt[%]	At.[%]
O K	2.43	3.54
F K	41.36	50.83
Cu L	2.50	0.92
Mg K	0.91	0.87
Al K	0.94	0.81
Si K	51.11	42.49
P K	0.55	0.42
K K	0.20	0.12
Total	100.00	100.00

The crystallinity, phase identification, lattice parameter, average crystallite size, and microstructure of lithium fluoride (LiF) prepared as thin films by the thermal evaporation deposition method and subjected to irradiation with gamma doses of 0 and 150 kGy, were analyzed by a Philips X'Pert Pro X-ray diffractometer.

The crystallinity, identification of the desirable LiF dominant phase, the lattice parameter, the average crystallite size, and the microstructure were determined after diffractograms of the LiF films were stripped using the Philips X'Pert HighScore Plus software. In order to improve the quality of the diffractograms, we opted for a low scan speed of 1.2°/min, a scan step of 0.02° in an angular range $2\theta \in 5°$–$120°$.

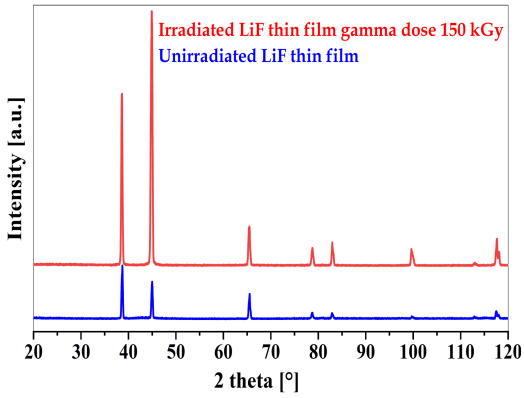

Fig. 10. Superposited diffractograms of unirradiated and gamma-irradiated LiF thin films.

In Fig. 10, a superposition of diffractograms of the unirradiated LiF samples, as well as the sample irradiated at 150 kGy, is shown. The observation of the diffractogram of unirradiated LiF shows the formation of two crystalline phases composed of the two elements of lithium (Li) and fluoride (F), which results in a splitting of the dominant peaks (see Table IV).

The diffractogram shows several peaks (08), including three (03) dominant peaks superimposed in an angular range of 35 to 120°, which are attributed to the two LiF phases of cubic "wurtzite" structure with two different lattice parameters, as well as a change of the preferential orientation. In the diffractogram of the LiF sample irradiated at a dose of 150 kGy, the complete absence of splitting and the appearance of a single, well-crystallized LiF phase are observed (JCPDS card No. 00-004-0857).

This phenomenon of beneficial phase modification (rearrangement of the material) can only be explained by the effect of gamma irradiation. Indeed, the preliminary results show well the effect of the gamma irradiation on the structure of LiF and, consequently, the elimination of the phase splitting, an improvement of the crystallinity, and an increase in the intensity with a widening of the peaks. Figure 11 shows the refinement of the diffractograms of the unirradiated and irradiated LiF samples using the Philips HighScore Plus software to identify the different diffraction peaks.

The average crystallite size was estimated by the Scherrer–Wilson formula [17–20]

$$D = \frac{K\lambda}{\beta \cos(\theta)}, \tag{20}$$

where D is the crystallite size (D [nm]), λ is the wavelength of the incident X-rays, θ is the diffraction angle (Bragg angle), and β is the width at half height (FWHM).

The calculated crystallite size values of the LiF films (unirradiated and irradiated) are given in Table V We found that the LiF samples (unirradiated and irradiated) show an average crystallite size at the nano-scale. The average crystallite

TABLE IV

Identification of the phases formed in unirradiated and gamma-irradiated LiF films.

Nature	Phases	Structure	Chemical formula	Reference JCPDS	Rate [%]
unirradiated	griceite	cubic	LiF	00-004-0857	55
	lithium fluoride			01-072-1538	45
irradiated	griceite	cubic	LiF	00-004-0857	100

TABLE V

Crystallite size values and micro-stresses of LiF nanoparticles (unirradiated and irradiated).

Thin film	Nature	Phases	Structure	$2\theta_{\text{int. peak}}$	Intensity [%]	Intensity [cts]	FWMM	hkl	d_{hkl} [Å]	D [nm]	ε [%]
unirradiated	griceite	LiF	cubic	38.599	78.87	837.20	0.178	111	2.33066	55.7	0.219
				44.898	57.69	612.36	0.202	200	2.01721	49.1	0.211
				65.530	45.70	485.09	0.171	220	1.42333	65.6	0.114
	lithium fluoride	LiF	cubic	38.752	100.00	1061.55	0.106	111	2.32179	106.6	0.127
				45.041	67.23	713.73	0.120	200	2.01114	92.5	0.123
				65.380	34.26	363.67	0.174	220	1.42624	64.2	0.117
Irradiated	griceite	LiF	cubic	38.591	65.56	3516.84	0.226	111	2.33111	42.3	0.280
				44.870	100.00	5364.08	0.303	200	2.01847	31.1	0.319
				65.398	15.07	808.24	0.272	220	1.42588	38.5	0.184

TABLE VI

Lattice Parameters and volume of the mesh of crystallized LiF nanoparticles before and after irradiation.

LiF nature	ICSD	Phase	Structure	$a = b = c$ [Å]	V [Å^3]
unirradiated	griceite	LiF	cubic	4.02945	65.42403
	lithium fluoride			4.03310	65.60198
irradiated	griceite	LiF	cubic	4.02899	65.40163

size D [nm] is calculated on the most intense peak hkl (200) located in the angular range 44–45° for the most stable LiF phase (JCPDS card No. 00-004-0857). A significant variation in crystallite size between the unirradiated and irradiated LiF samples can be observed.

Indeed, we note a significant modification of the average diameter of the crystals of the unirradiated LiF sample calculated at about 49.1 nm decreases to about 31.1 nm for the irradiated LiF sample. Concerning the second LiF phase, formed in the case of the unirradiated sample (JCPDS card No. 01-072-1538), we note that the size of the crystallites is important, reaching up to 100 nm on the more stable phase, calculated from the most intense peak hkl (111), located in the angular range of 38–39$^c icr$. For the calculation of the lattice parameter, we used the rule of (07) crystal systems and the 14 types of Bravais lattices. We deduced that d_{hkl} of the cubic lattice is written according to the following relation

$$d_{hkl} = \frac{a}{\sqrt{h^2 + k^2 + l^2}}. \tag{21}$$

In Table VI, the values of the mesh parameters and the mesh volume V [Å^3] of the LiF phases forming our two samples of unirradiated and irradiated LiF are given.

Preliminary results clearly indicate the contribution of the effect of gamma irradiation (150 kGy) causing a slight variation of the lattice parameter a [Å] of the most stable well-crystallized phase of LiF (JCPDS card No. 00-004-0857), as well as a slight decrease of the lattice volume, which shows a good correlation between the lattice volume V [Å^3] and the lattice parameter a [Å] due to the cubic structure of LiF. This phenomenon has been explained in detail by several authors [21, 22] who studied the effect of irradiation at room temperature using a cobalt-60 (^{60}Co) gamma source. They found that irradiation at a dose higher than 100 kGy has the effect of increasing the electrical conductivity and concluded that gamma irradiation causes electronic decoration and/or inhibition of defects by an association of defects (Mg^{++} with Li^{+}) responsible for sources of conductivity vacancies, which is interpreted as a mechanism of material healing. The samples are considered to be very pure, as their electrical conductivity in the non-intrinsic range is about a thousand times lower than the conductivity of ordinary samples, whose impurity content does not exceed 10^{-4}, so gamma irradiation has the effect of increasing its conductivity by adding a charge.

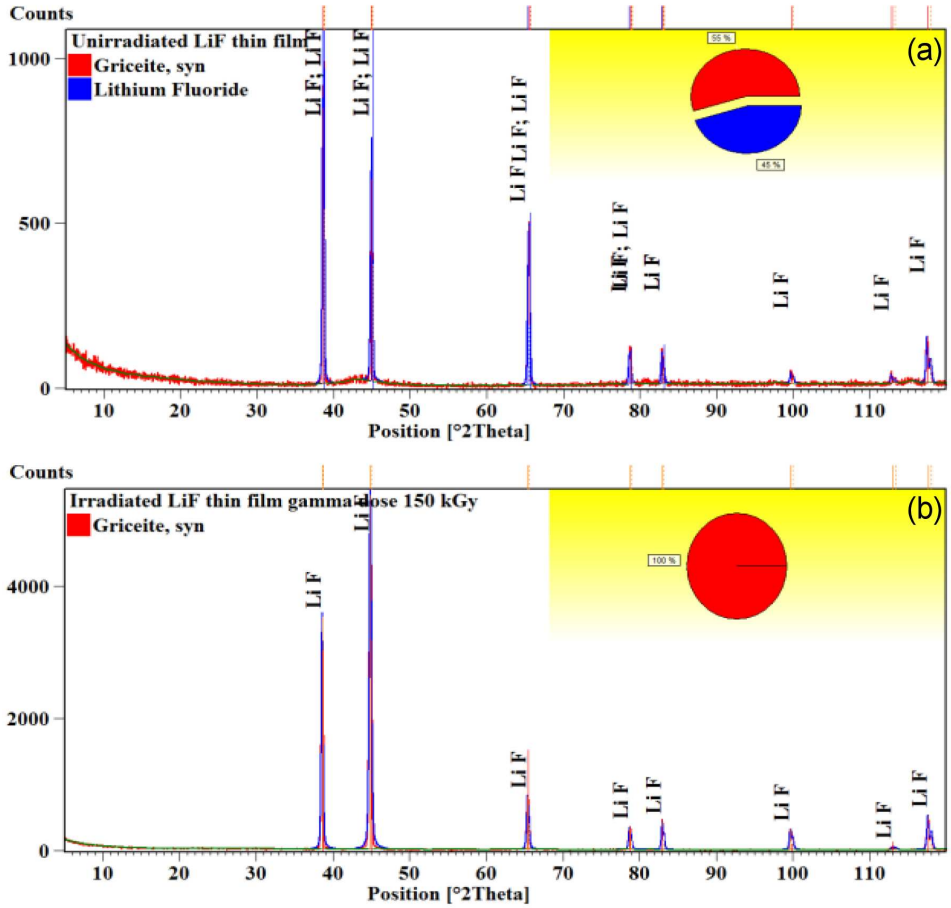

Fig. 11. Adjustment of unirradiated and irradiated LiF nanoparticle diffractograms by Philips HighScore Plus software.

3. Measurements

We opted for a simple design of a neutron detector model consisting of a single Schottky surface barrier silicon detector (Si-SBD-$_{2cm\times2cm\times300\mu m}$), fabricated and characterized previously, associated with different films of neutron converter (^{6}LiF) of optimized thicknesses, deposited on the active surface by the thermal evaporation deposition method. The distance between the ^{6}LiF thin films and the surface of the silicon detector is practically zero. This configuration has the advantage of not requiring correction of the detection efficiency since the majority of the ^{6}Li reaction particles penetrate the silicon detector. Its other advantage is the simplicity of installation, which is practical and allows the detector to be replaced as many times as necessary with others with different thicknesses of ^{6}LiF films [23, 24]. For protection against stray radiation, the silicon detector with the ^{6}LiF thin films is inserted into a Teflon cylinder (Fig. 12).

A silicon detector, alone or with films of ^{6}LiF, is fixed inside a box and then wrapped in aluminum foil. The box is placed at a distance of 100 cm in front of the window of the AmBe neutron irradiation source (OB26.SSDL/CRNA) and surrounded

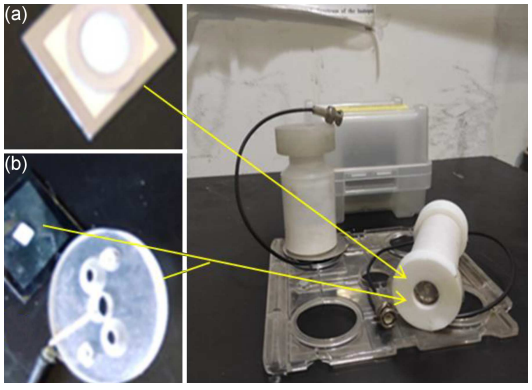

Fig. 12. Neutron Detector model (a) Si-SB/^{6}LiF thin films and (b) Si-SB/^{6}LiF pellets.

by polyethylene plates. Polyethylene was necessary to attenuate the original neutron spectrum of the neutron source, which extends from up to 10 MeV to lower energy (thermal 0.025 eV). The measurement time was set to 1200, 3600, or 10000 s for better counting statistics, and the measurements are given in counts per second (cps). The source used is an AmBe/OB26 (Fig. 13), a neutron source,

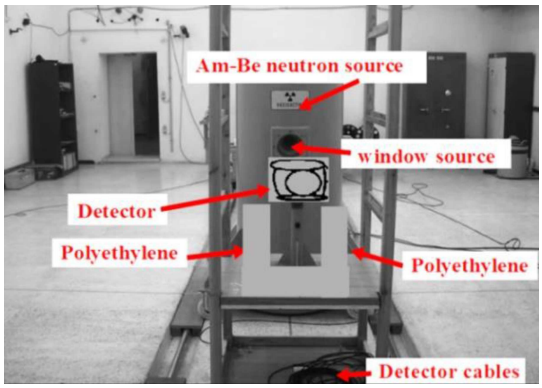

Fig. 13. General view of the OB[26] neutron irradiator inside the Algerian secondary standard dosimetry laboratory (SSDL-CRNA-Algeria).

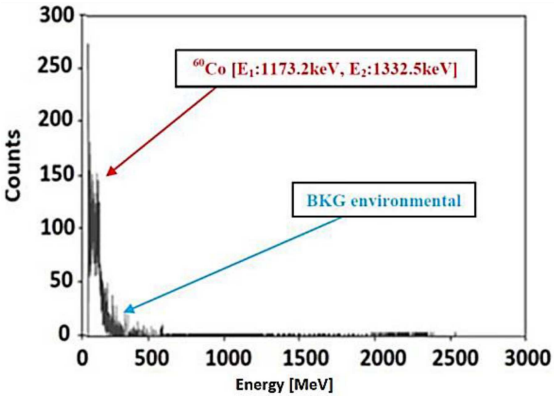

Fig. 14. Environmental background and spectrum of the ^{60}Co gamma source, measured with [Si-SBD$_{2cm\times2cm\times300\mu m}$] on ^{6}LiF film of 2$\mu$m of thickness.

and it produces a thermal neutron flux of about 1.106 n s/cm^2 and emits a considerable number of low-energy gamma rays of 59.5 keV from ^{241}Am and as many high energy gamma rays (4.4 MeV) from the alpha-Be reaction. Simulation work has been undertaken on the source [25–29].

3.1. Background and gamma source

The first measurements were devoted to the evaluation of the detector behavior when exposed to environmental background or gamma doses from a cobalt-60 (^{60}Co) source [30]. Measurements were carried out on the detector [Si-SBD$_{2cm\times2cm\times300\mu m}$], fabricated and previously calibrated, with and without a film of ^{6}LiF with a thickness of 2 μm. The measurement spectra are shown in Fig. 14.

The measurement spectrum shown in Fig. 14 indicated that there is no significant influence of BKG. All the data are clustered on the low-energy part $<$ 200 keV, similarly the irradiations with the ^{60}Co gamma source, and show a slight shift in the amplitude of the spectrum at about 650 keV, far

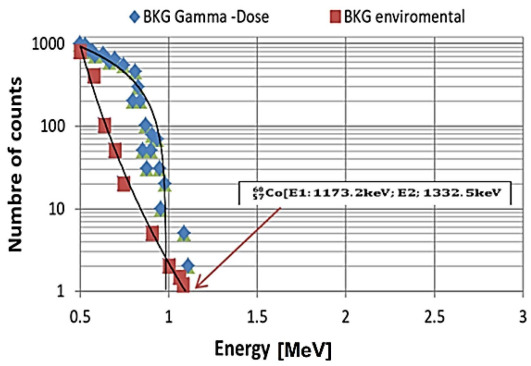

Fig. 15. Graphical representation of the background environmental red spectra and gamma dose background from the ^{60}Co source black spectra.

from the maximum energies of the ^{60}Co source (E_1 = 1173.2 keV and E_2 = 1332.5 keV), as schematically represented in Fig. 15. This result confirms that there is no significant effect of gamma doses on the ^{6}LiF thin films or on the silicon detector.

3.2. Neutron energy spectra measured at different thickness of LiF film

We started a series of measurements with a silicon detector [Si-SBD$_{2cm\times2cm\times300\mu m}$] without a film and with a 0.5 μm film of ^{6}LiF. We collected the neutron energy spectrum and then repeated the measurements for other ^{6}LiF film thicknesses (0.5 μm and 1 μm). The measurement spectra are shown in Fig. 16.

In Fig. 16, the response of the detector at 0.5 and 1μm is presented, and the shape of the spectra is explained by exothermic thermal neutron reactions with the ^{6}Li nucleus, giving two characteristic peaks — a hump-shaped peak at about 2.34 MeV and a peak at about 2.01 MeV, presumably belonging to the energies of (^{3}H) and α particles, produced by the nuclear reaction ^{6}Li(n, α)^{3}H; E_{3H} = 2.73 MeV, E_α = 2.05 MeV. For a better interpretation, we have plotted all the measurement spectra on the same chart and introduced an energy threshold to filter only the counts above this threshold (Fig. 17). It is also possible to define an energy window of 1.57 MeV [31].

A series of measurements were carried out with a detector [Si-SBD$_{2cm\times2cm\times300\mu m}$] and 4 μm thick ^{6}LiF targets, made in pellet form from ^{6}LiF powder. We collected neutron energy spectra as a function at 4 μm^{6}LiF thickness shown in Fig. 16.

Observation of the spectra in Fig. 16 (4.0 μm) indicates that the spectra present the two characteristic peaks, which are in the vicinity of energies of 2.55 MeV and 1.50 MeV, consistent with the particle energies of $E(^{3}H)$= 2.73 MeV and

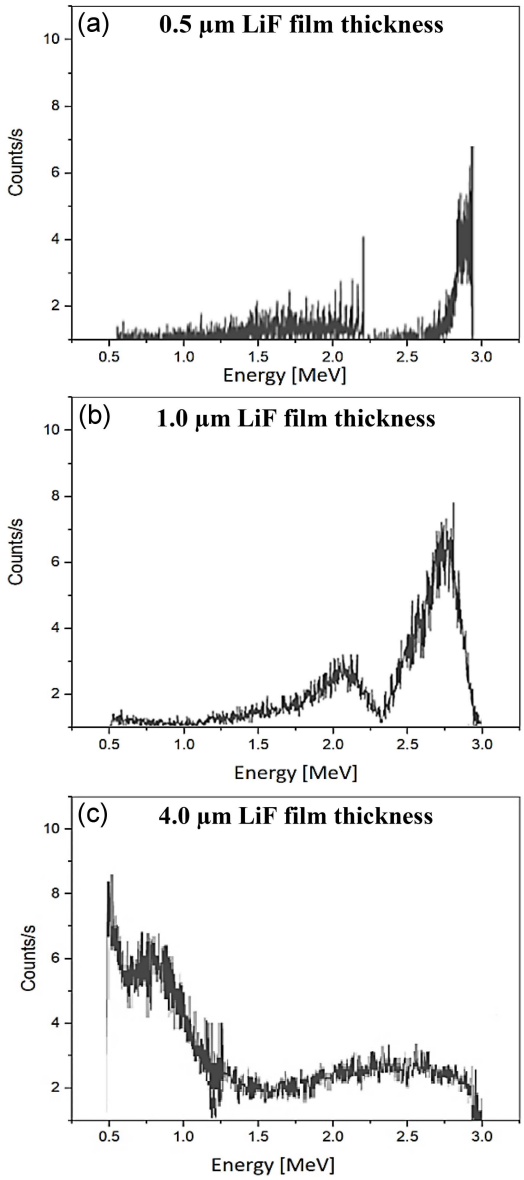

Fig. 16. Neutron energy spectra measured with [Si-SBD$_{2\text{cm}\times2\text{cm}\times300\mu\text{m}}$] on different thickness of LiF films (0.5, 1, and 4 μm).

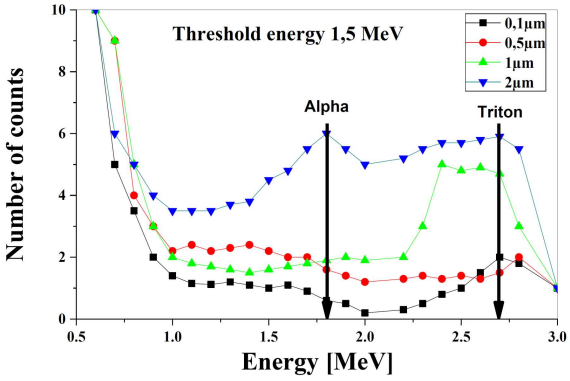

Fig. 17. Neutron energy spectra of the AmBe source with [Si-SBD$_{2\text{cm}\times2\text{cm}\times300\mu\text{m}}$] detector and different thicknesses of ^{6}LiF films with threshold energy of 1.5 MeV grouped on the same graph.

TABLE VII

Neutron detector response as a function of LiF film thickness.

	Film thickness [μm]					
	0.5	1	2	3	4	5
neutron coints [cps]	9	15	33	75	110	150
BKG counts [cps]	0.19	0.15	0.15	0.17	0.19	0.15
average efficience E [%]	0.24	0.75	1.23	1.51	1.83	2.01
energy resolution R [keV]	88	110	145	187	246	288
sensitivity on the ^{3}H peak [cps]	10 ± 0.1					
gamma BKG [cps]	$> 10^{-6}$					

$E(\alpha) = 2.05$ MeV, products of the ^{6}Li(n, α)^{3}H reaction. The region ratio (alpha/triton) corresponds to an approximate yield of 2.5%, which is consistent with literature data [32, 33]. For a better analysis of the spectra, for each thickness of the ^{6}LiF target, we will have to define an energy threshold to consider only neutrons with energy above.

The choice of the threshold is a trade-off between the efficiency and the background in order to allow a better evaluation of the effect of the thickness increase on the variation of the efficiency. In this work, we decided to set an energy window between 1.5 MeV and 2.7 MeV for all ^{6}LiF thicknesses, and the measurement values are given in Table VII.

Table VII shows all the measurement values in terms of the number of neutron counts per second detected (cps) as a function of different thicknesses of the ^{6}LiF film, the background, and the counting ratio of the substrate without and with thin films, in an energy window of 1.57–2.70 MeV. A first reading of the results (Table VII) showed a significant influence of the gamma doses on the detector, which increases the background rate. This was explained by the different mechanisms of gamma radiation interactions (Compton effect, photoelectric effect, or pair creation) and/or by other effects that intervene, such as the interaction of fast neutrons on the silicon detector that surrounds the ^{6}LiF target.

In order to facilitate the comparison of all the measurements according to the different thicknesses of the ^{6}LiF thin films, we have plotted all the measurement spectra on the same graph for better analysis and interpretation of the results (Fig. 18). We have introduced an energy threshold, for which we will only consider neutron counts above this threshold and reject neutron energy counts below the energy threshold [33]. The energy threshold, set at $E_s = 1.57$ MeV, was chosen as a compromise between the detection efficiency and the background value, defined in an energy range of 1.5–2.73 MeV.

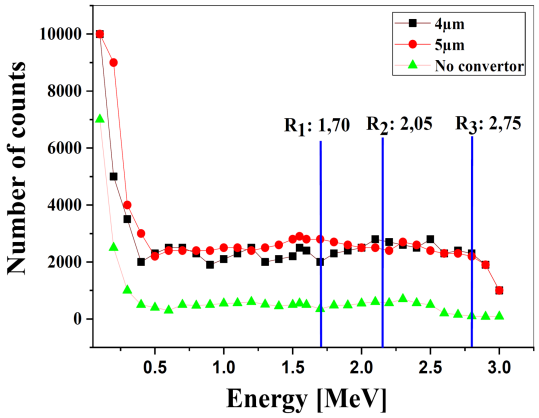

Fig. 18. Neutron energy spectrum measured with [Si-SBD$_{2cm\times 2cm\times 300\mu m}$] on different thicknesses of ^{6}LiF film in 1.5–2.7 MeV range energy.

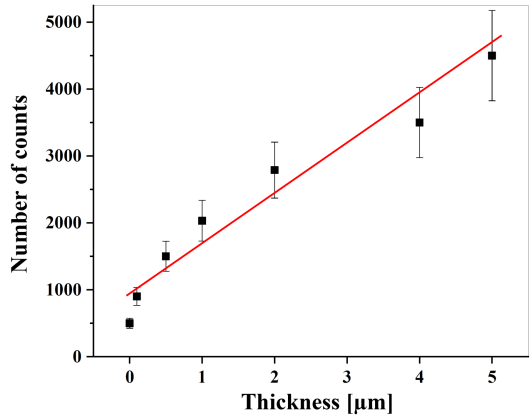

Fig. 19. Variation of the detection efficiency with increasing ^{6}LiF thin films thickness.

This will allow us to interpret and judge the effect of increasing the thickness of the ^{6}LiF thin films on the variation of the detection efficiency, according to the SRIM calculation code [34].

The energy loss of particles passing through ^{6}LiF thin films corresponds to 10 μm for α particles with energy $E_\alpha = 2.05$ MeV and 30μm for triton particles with energy $E_{3H} = 2.7$ MeV, which is in agreement with our experimental values (an energy loss evaluated at 5.82 μm for alpha particles with energy 2.05 MeV and 32.5 μm for tritons particles with energy 2.73 MeV) of the ^{6}Li(n, α)^{3}H reaction products. We noticed that beyond a thickness of 2 μm, the maximum amplitude of the (^{3}H) particle is higher than the maximum amplitude of the (α) particle.

This can be explained by the fact that the heavier alpha particle deposits the maximum energy at the beginning of the thin films, resulting in a short lineal distance and therefore fewer interactions, whereas the lighter (^{3}H) particle is more penetrating, resulting in a long lineal distance and therefore more interactions. Although the energies of the particles in the ^{6}Li(n, α)^{3}H reaction might be expected to match the maximum energies of the spectrum, this is not the case for all thin film thicknesses. Indeed, in the case of thin films (4 μm), we notice that most of the newly formed charged particles stop in the epitaxial thin films of the silicon detector, where we observe three distinct regions: 1.1–1.5 MeV, 1.5–2.0 MeV, and 2.4–2.7 MeV [35–37].

- Region 2.4–2.7 MeV — possibly attributed to (^{3}H) particles, the curve forms a Gaussian with a well-defined maximum, which corresponds to the moment when all the ^{3}H particle energy is deposited in the epitaxial thin films, merging with the maximum tritium energy of the ^{6}Li reaction.
- Region 1.5–2.0 MeV — possibly attributed to alpha particle energy. It can also be assumed that when all the energy is deposited in the epitaxial thin films, it corresponds to the energy of ^{6}Li alpha particles.
- Region 1.1–1.5 MeV — possibly attributed to (^{3}H) particles and probably to low-energy alpha particles. However, this region may be more indicative of tritium particles only since, in this energy range, it is mainly (^{3}H) energy that is gradually deposited.

In the case of thick thin films (2 μm), we notice that the first region increases, and conversely, the second region decreases. This can be interpreted as follows — when the thickness increases, the phase particles have difficulty crossing the thin films, and one can no longer distinguish the end of the shift curve of the phase particles. On the other hand, in the second region, it merges with the third, i.e., with the region attributed to the ^{3}H particle, which indicates that at this thickness the majority of the particles have deposited their maximum energies in the thin films.

3.3. Detection efficiency

The detection efficiency of the neutron device was deduced from the total number of neutron hits as a function of different ^{6}LiF film thicknesses. Figure 19 shows that the variation in detection efficiency is a consequence of the increase in thin film thickness because of self-absorption. This has been reported by many authors [38–40]. The amplitude of the maximum attributed to the particles of tritium is greater than the amplitude of the maximum attributed to the energy of the alpha particle, this is explained by the fact that the alpha particle is heavier and therefore has a low free path in the material, therefore, causes fewer interactions than the much lighter ^{3}H triton particle causes more interactions. The average detection efficiency has been estimated to be about 0.75% for film thicknesses $\sim$ 1 μm. The energy resolution is much better for

vacuum measurements, as the spectra are shifted to higher energies due to less energy deposition in the air. The rate of charged particles in the air is about $\sim$ 70 mm for ^{3}H at the time of vacuum irradiation. The distance (d) (thin films to the active surface) is close to zero due to the direct deposition of ^{6}LiF on the detector surface. In this configuration, even in the absence of a vacuum, all the charged particles produced in the ^{6}LiF reach the detector.

4. Conclusions

This work aims to find new methods of neutron spectrometry as an alternative to the ^{3}He gas detector. The obtained results clearly show the feasibility and certainty of a viable alternative method insensitive to gamma rays. A model neutron detector was designed based on the fabrication of a silicon semiconductor detector with a Schottky surface barrier [Si-SBD$_{2\text{cm}\times2\text{cm}\times300\mu\text{m}}$] combined with a neutron converter film (^{6}LiF) and deposited on its active surface by the vacuum joule thermal evaporation method. The detector [Si-SBD$_{2\text{cm}\times2\text{cm}\times300\mu\text{m}}$/^{6}LiF] showed an appreciable detection efficiency of the order of 1% for a film thickness of 2 μm. The characteristics obtained as a function of different ^{6}LiF film thicknesses (Table VII) prove that the variation in detection efficiency is a consequence of the increase in the thickness of the ^{6}LiF thin film. Indeed, the increase in thickness tends to increase the macroscopic neutron cross section, and thus, more charged particles reach the detector, resulting in a gain in efficiency. On the other hand, a deterioration in energy resolution has been observed due to the loss of particle energy (α) by a self-absorption effect when passing through the film, thus, part of the particle energy (α) is lost in the background, and part of the particle energy (^{3}H) is shifted to the alpha energy region, as reported by several authors [36–38]. The different tests were carried out (BKG detector, BKG gamma, detector with different ^{6}LiF films, detector with different ^{6}LiF targets wrapped in a polymer film) with an AmBe neutron source (0B26-SSDL), which allowed us to carefully evaluate these performances and to shed light on the contribution of the contact materials, as well as other nuclear reactions that can occur on the ^{6}LiF and on the silicon detector, and we have shown that this contribution can be neglected or taken into account. For a better evaluation of the performance of this type of neutron detector, a series of tests was performed on a single detector associated with a 0.5 μm thick ^{6}LiF mono-film. The analysis of the obtained neutron spectrum was done by selecting the peak of (^{3}H) corresponding to a threshold energy of 1.7 MeV in an energy window of 1.5–2.7 MeV. Knowing the thickness and thermal neutron absorption cross section of the ^{6}Li contained in ^{6}LiF and considering the count on the ^{3}H peak (cps), the average detection efficiency was estimated to be $\sim$ 0.22% (including the angular efficiency at the emission of (^{3}H) at large angles deep into the ^{6}LiF). Using this data, we deduce approximately the number of thermal neutrons that reach the detector at $\sim$ 3000 n/s. From these preliminary results, we can judge the performance of our detector [Si-SBD$_{2\text{cm}\times2\text{cm}\times300\mu\text{m}}$/^{6}LiF-0.5 μm] when using a stack of 0.5 μm thick thin films. The maximum detection efficiency is reached ($\sim$ 1%) when using 1 μm thin films and 2μm (4 $\times$ 0.5 μm) thin films of ^{6}LiF, successively deposited on the active surface of the detector by thermal evaporation. The significant contribution of background noise to the silicon detector, attributed to the interaction of fast neutrons from the Am-Be source, cannot be neglected. This means that the detector is also sensitive to fast neutrons and various other interaction mechanisms, however, with good neutron thermalization, this effect can be reduced or even eliminated. As for the gamma-ray sensitivity, it is lower than 10^{-6} for a ^{60}Co source, therefore, from a gamma/neutron rejection point of view, the detector can be considered equivalent to a ^{3}He gas detector. The flat geometrical structure of the detector makes it easy to deduce its efficiency once the ^{6}LiF film is deposited and its thickness is known. Worth mentioning are the low voltage operation, which considerably simplifies the use of the detector, as well as its very simple mechanical structure and the absence of gas for its operation (^{3}He gas). The great advantage of this model of the detector is that it can be designed and produced in large quantities in different shapes and sizes and at low cost. Finally, our work continues to improve the performance (efficiency) of this detector design, with a maximum gamma/neutron rejection rate comparable to that of the ^{3}He gas neutron detector.

Acknowledgments

We address our sincere thanks to M. A. Keffous, Director of the CRTSE, who allowed me to carry out this work, and also to M.J. Bentayeb (USTHB), Mme. S. Brahimi-Kaloune (CDTA) and Mme S. Brahimi-Moussa (USD-Blida) for their help and their moral support.

References

[1] R.T. Kouzes, J.H. Ely, L.E. Erikson, W.J. Kernan, A.T. Lintereur, E.R.Siciliano, D.L. Stephens, D.C. Stromswold, R.M.V. Ginhoven, M.L. Woodring, *Nucl. Instrum. Methods Phys. Res. A* **623**, 1035 (2010).

[2] Y. Liu, Y. Yang, Y. Tai, Z. Zhang, *Chin. Phys. C* **40**, 076201 (2016).

[3] H. Mazrou, T. Sidahmed, M. Allab, *Radiat. Prot. Dosim.* **141**, 114 (2010).

[4] H. Geissel, H. Weick, C. Scheidenberger, R. Bimbot, D. Gardès, *Nucl. Instrum. Methods Phys. Res. B* **195**, 3 (2002).

[5] S. Pospisil, B. Sopko, E. Havrankova, Z. Janout, J. Konicek, I. Macha, J. Pavlu, *Radiat. Protect. Dosim.* **46**, 115 (1993).

[6] G. Ko, H.Y. Kim, J. Bang, J. Kim, *J. Korean, Chem. Eng.* **26**, 285 (2009).

[7] G. Cote, *Analysis* **17**, 55 (1989).

[8] A. Keffous, M. Siad, A. Cheriet, Y. Belkacem, Y. Boukennous, K. Bourenane, A. Maallemi, H. Menari, W. Chergui, *Vacuum* **80**, 908 (2006).

[9] N. Gabouze, A. Keffous, T. Kerdja, Y. Belaroussi, *Appl. Surf. Sci.* **255**, 6751 (2009).

[10] F.S. Goulding, W.L. Hansen, *IEEE Trans. Nucl. Sci.* **11**, 286 (1964).

[11] D.S. McGregor, J.E. Kammeraad, *Semicond. Semimetals* **43**, 383 (1995).

[12] E. Belau, J. Kemmer, R. Klanner, U. Kötz, G. Lutz, W. Männer, E. Neugebauer, H.J. Seebrunner, A. Wylie, *Nucl. Inst. Methods* **217**, 224 (1983).

[13] V. Lohrabian, A. Kamali-Asl, H.G. Harvani, S.R.H. Aghdam, H. Arabi, H. Zaidi, *Radiat. Phys. Chem.* **189**, 109666 (2021).

[14] A. Vivier, G. Lopez, Cross section of the reaction ^{6}Li et ^{7}Li, Programme DOSIMEX-N 2.0, 2015.

[15] S.L. Meo, L. Cosentino, A. Mazzone, P. Bartolomei, P. Finocchiaro, *Nucl Instrum. Methods Phys. Res. A* **866**, 48 (2017).

[16] A. Tumino, C. Spitaleri, C. Bonomo, S. Cherubini, P. Figuera, M. Gulino, M. La Cognata, L. Lamia, A. Musumarra, M.G. Pellegriti, R.G. Pizzone, A. Rinollo, S. Romano, *Eur. Phys. J. A* **25**, 649 (2005).

[17] B. Rahal, B. Boudine, Y. Larbah, M. Siad, N. Souami, *J. Inorg. Organomet. Polym. Mater.* **31**, 4001 (2021).

[18] Y. Larbah, M. Adnane, B. Rahal, *Semiconductors* **54**, 1439 (2020).

[19] B. Rahal, B. Boudine, Y. Larbah, L. Guerbous, M. Sebais, O. Halimi, M. Siad, *J. Opt. Int. J. Light Electron Opt.* **169**, 303 (2018).

[20] B. Rahal, B. Boudine, A.R. Khantoul, M. Sebais, O. Halimi, *J. Opt. Int. J. Light Electron Opt.* **127**, 6943 (2016).

[21] P. Bergé, G. Blanc, *Bulletin de la Société française de Minéralogie et de Cristallographie* **83**, 257 (1960).

[22] M. Lambert, Ch. Maziére, A. Guinier, *J. Phys. Chem. Solids* **18**, 129 (1961).

[23] F. SEITZ, S.R. KOEHL, *Solid State Physics*, Academic Press Inc., 1956.

[24] D. Benzaid, A. Seghour, A. Borras, *Int. J. Mod. Phys. E* **26**, 1750058 (2017).

[25] A. Seghour, J.C. Sens, *Nucl. Instrum. Methods Phys. Res. A* **420**, 243 (1999).

[26] ISO 8529-1:2021, "Neutron Reference Radiations Fields — Part 1: Characteristics and Methods of Production", 2001.

[27] M. Reginatto, P. Goldhagen, S. Neumann, *Nucl. Instrum. Methods A* **476**, 242 (2002).

[28] H. Mazrou, Z. Idiri, T. Sidahmed, M.Allab, *J. Radioanal. Nucl. Chem.* **284**, 253 (2010).

[29] H. Mazrou, T. Sidahmed, M. Allab, *Radiat. Prot. Dosim.* **141**, 114 (2010).

[30] OPRI/INRS, Cobalt-60, *Radiation Protection Data Sheet for the Use of Radionuclides in Unsealed Sources*, 1996.

[31] R. Sarraf-Mamoory, S. Nadery, N. Riahi-Noori, *Chem. Eng. Commun.* **194**, 1022 (2010).

[32] J. Schelten, M. Balzhäuser, F. Höngesberg, R. Reinartz, *Phys. B Condens. Matter* **234**, 1084 (1997).

[33] X. Duan, D. Yang, Z. Sunand, H. Sun, *J. Cryst. Growth* **252**, 4 (2003).

[34] M.J. Berger, J.S. Coursey, M.A. Zucker, J. Chang, ESTAR, PSTAR, and ASTAR: (ver. 1.2.3), Code SRIM2013 (J.P. Biersack, J.F. Ziegler) 2005.

[35] A. Massara, S. Amaducci, L. Cosentino, F. Longhitano, C. Marchetta, G.E. Poma, M. Ursino, P. Finocchiaro, *Instruments* **7**, 1 (2023).

[36] A.L. Giudice, F. Fasolo, E. Durisi, C. Manfredotti, E. Vittone, F. Fizzotti, A. Zanini, G. Rosi, *Nucl. Instrum. Methods Phys. Res. A* **583**, 177 (2007).

[37] R.W. Flammang, J.G. Seidel, F.H. Ruddy, *Nucl. Instrum. Methods Phys. Res. A* **579**, 177 (2007).

[38] Q. Li, G. Luan, J. Bao, J. Tang, R. Fan, H. Bai, *Nucl. Instrum. Methods Phys. Res. A* **946**, 16249 (2019).

[39] A. Soto, R.G.Fronk, K. Neal, B. Ehresmann, S. L.Bellinger, M. Shoffner, D.S. McGrego, *Nucl. Instrum. Methods Phys. Res. A* **966**, 163852 (2020).

[40] J. Coutinho, V.J.B. Torres, I. Capan et al., *Nucl. Instrum. Methods Phys. Res. A* **986**, 164793 (2020).